# Qualitative and Quantitative Improvement of Optical Tomographic Reconstructed Images via Spatial Deconvolution: Three–Dimensional Case

H. L. Graber[1,2], Yong Xu[1,2], Y. Pei[1], and R. L. Barbour[1,2]

[1]*SUNY Downstate Medical Center and* [2]*NIRx Medical Technologies, LLC.*

## INTRODUCTION

In diffuse optical tomography (DOT) applications, reconstructed images frequently exhibit undesirable features such as blurring and location bias. At least two basic factors underlie these phenomena. First, there must be an inherent limit on the image quality that is ultimately achievable [1]. Second, they may be consequences of steps that are taken to counter the effects of noise in detector data (e.g., regularization) or to ensure stability and/or accelerate convergence of the inverse problem (e.g., matrix scaling). Distortion of spatial information and low spatial resolution thus can arise as difficult-to-avoid tradeoffs from operations that allow one to solve the inverse problem at all. While for any particular problem it may be possible to find optimal control-variable values that will maximize the qualitative spatial accuracy and the quantitative accuracy of a recovered image, generally applicable and computationally tractable strategies for doing so have been lacking. Here, it is shown that a technique first developed as a tool for directly assessing the action of image reconstruction algorithms [2] can, when suitably modified, serve as such a tool for enhancing the quality of reconstructed images.

The method described below grew out of our previously reported work on the topic of distinguishing absorption from scattering perturbations in media when conducting steady-state optical tomographic studies [3,4]. In cases where the test medium had spatially coincident absorption and scattering perturbations, the reconstruction algorithm's ability to separate them was assessed by assigning a qualitatively different form of temporal fluctuation to each optical parameter. These dynamics acted as tags by which inter-parameter crosstalk was precisely quantified [5]. While that work was in progress, it was recognized that the tagging of optical parameters with temporal information immediately suggests a general mechanism for characterizing the action of DOT image reconstruction algorithms on their input data. Namely, let a distinct mode of temporal fluctuation be assigned to each optical parameter of interest in every volume element of a medium, and let a time series of forward and corresponding inverse problem solutions be computed. Then a map of magnitude vs. location for a given mode of fluctuation within the image space reveals precisely how the reconstruction algorithm distributes the corresponding optical parameter throughout that space. An illustrative example of this is shown in Figure 1. A mapping from object to image space obtained in this way is conceptually analogous to a point spread function (PSF) [6],which characterizes the physical accuracy and resolution of an optical device. In view of this analogy, the term information spread function (ISF) has been adopted as our descriptor for the type of object-space to image-space mapping described here. The ISF formulation has an important implication that provides the main topic of the present report. Namely, once the behavior of a reconstruction algorithm has been characterized under a given set of initial conditions (i.e., for a particular reference medium and arrangement of sources and detectors), its ISFs can be used in deconvolution computations, to improve the spatial resolution and accuracy of reconstructed images. This application is entirely analogous to the established practice of using the PSFs of an optical measuring device as the basis for a calibration/correction procedures to reduce image blurring and/or aberrations [7,8]. Results presented below demonstrate that highly significant improvements in the quality of DOT image spatial information can be achieved in this way. Also worth stressing is that the technique described here can be applied to media of arbitrary shape and internal composition, and arbitrary source-detector geometries, in a computationally efficient manner.

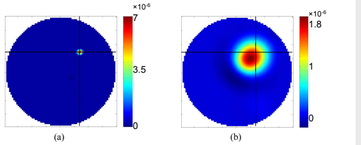


**Figure 1.** (a) – spatial map of amplitude of one selected temporal model function, assigned to the absorption coefficient ($\mu_a$) of a FEM mesh node located at the intersection of the horizontal and vertical black lines. In this illustrative example, the mesh is a 2D disc with homogeneous $\mu'_s$, while each node's $\mu_a$ has a time-dependence, the temporal average value of $\mu_a$ is spatially homogeneous. (b) – spatial map of amplitude, in the time series of reconstructed $\mu_a$ images, of the same temporal frequency as that uniquely assigned to the indicated FEM mesh node in 1(a).

## METHODS

### 1. Image Correction Algorithm (Spatial Deconvolution)

An important limitation of DOT is that is that first-order solutions to linear perturbation problems often produce less than ideal solutions, with image blurring evident. A fundamental premise of this work is that, as shown schematically if Figure 2(a), the most important underlying factor is *linear* spatial convolution, or mixing of information from many target medium locations in any given image pixel or voxel. Our goal was to derive a mathematical operator (or "filter") that whose effect, as sketched in Fig. 2(b), is to reduce this mixing effect as much a possible, producing a final image that comes as close as possible to a one-to-one correspondence between object and image pixels.

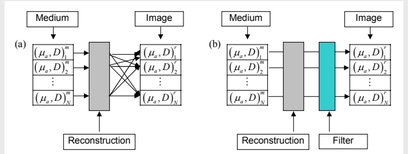


**Figure 2.** Panel A, schematic depicting the action of typical DOT image reconstruction algorithm, which yields blurred images because information from each object domain location is mapped to more than one position in the image domain. Panel B, the action of an ideal image-correcting filter, which is to counteract the information spreading aspect of the reconstruction algorithm's action.

The strategy we have developed was conceptually motivated by a consideration of the physical basis of image formation in MRI. There, spatial discrimination is possible because the imposition of a magnetic field gradient creates a range of position-dependent resonance frequencies. This same concept is applied here to the image formation problem of optical tomography. It is implemented, as shown schematically in Figure 3, by tagging the absorption coefficient ($\mu_a$) in every object pixel with a unique time-varying function. (While the reduced scattering coefficient ($\mu'_s$) may be simultaneously tagged in the same way, in order to assess the degree of inter-parameter crosstalk in the recovered images, to simplify the presentation only $\mu_a$ was modulated in the examples presented here. In the implementation that was used to produce said results, the tagging functions used were simple sine waves with incommensurable frequencies.

**Figure 3.**

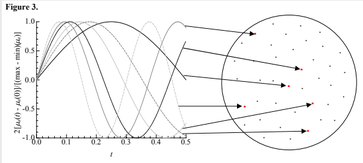


1) Assign a modulation frequency to each element's $\mu_a$.
2) Forward problem: compute $N_f$–time–point measurement time series, with $N_f > 2\max(f_{mod})\text{/}\min(\Delta f_{mod})$
3) Inverse problem: reconstruct time series of $N$ tomographic images [9]
4) Post–processing: from matrices of medium's $\mu_a$ states and corresponding reconstructed images ($\mathbf{M}^{\mu a}$ and $\mathbf{M}'$, respectively), compute image correction filter, $\mathbf{F}$, by solving $\mathbf{M}^{\mu a} = \mathbf{FM}'$ [10].

## METHODS (cont.)

After the first three steps outlined in Fig. 3 are completed, ISFs such as that in Fig. 1 can be produced by computing the correlations between the reconstructed image time series and each of the functions used as pixel tags. Alternatively, by computing the power spectra of each pixel's reconstructed $\mu_a$ time series, if the tagging functions are sinusoidal as they are here. If each map of the type in Fig. 1(b) is rearranged as a 1D vector, using a consistent numbering scheme for the pixels, then the ISFs for all $N_p$ pixels ($N_p$ = 717 in the particular case illustrated here) can be displayed in a single 2D gray-scale map. An example, for the medium in Fig. 1, is shown in Figure 4. In the absence of spatial convolution effects, this map would have non-zero values only along the main diagonal. The finite width of the band of gray dots straddling the diagonal in Fig. 4 is a manifestation of blurring, while the absence of perfect symmetry about the diagonal shows that many medium pixels also have a location bias in the images, of the type seen in Fig. 1(b).

The procedure we use to correct these errors, outlined in the fourth step of Fig. 3, merits a more detailed mathematical description. The hypothesis sketched in Fig. 2(a) is that the apparent value in each pixel of a reconstructed image is a linear combination of the information in all medium pixels. If the numerical factors describing the contribution of every medium pixel to each image pixel were known, they could be arranged as a matrix that in principle could be inverted, allowing us to recover the true spatial distribution of medium $\mu_a$s by a straightforward matrix multiplication:

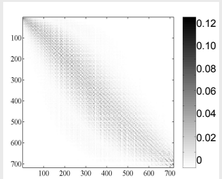


**Figure 4.** 2D matrix representation of reconstructed amplitude spatial maps (see Fig. 1(b)), for all pixels in the medium shown in Fig. 1. In this representation, each row corresponds to one pixel in the original medium, and each column to one pixel in the reconstructed image space.

$$\begin{bmatrix} \mu_{a1}^{m} \\ \mu_{a2}^{m} \\ \vdots \\ \mu_{aN_p}^{m} \end{bmatrix} = \begin{bmatrix} f_{11} & f_{12} & \cdots & f_{1N_p} \\ f_{21} & f_{22} & \cdots & f_{2N_p} \\ \vdots & \vdots & \ddots & \vdots \\ f_{N_p1} & f_{N_p2} & \cdots & f_{N_pN_p} \end{bmatrix} \begin{bmatrix} \mu_{a1}^{r} \\ \mu_{a2}^{r} \\ \vdots \\ \mu_{aN_p}^{r} \end{bmatrix} \quad (1)$$

or $\boldsymbol{\mu}_a^m = \mathbf{F}\boldsymbol{\mu}_a^r$. An equation having the form of Eq. (1) can be written for each of the $N_f$ states of the medium. If the modulation amplitudes in all medium pixels are not large, it is reasonable to further assume that $\mathbf{F}$ is the same in all of the $N_f$ resulting equations. Then they may be combined into a single linear system,

$$\left[\boldsymbol{\mu}_a^{m(1)} \middle| \boldsymbol{\mu}_a^{m(2)} \middle| \boldsymbol{\mu}_a^{m(3)} \middle| \cdots\right] = \mathbf{F}\left[\boldsymbol{\mu}_a^{r(1)} \middle| \boldsymbol{\mu}_a^{r(2)} \middle| \boldsymbol{\mu}_a^{r(3)} \middle| \cdots\right], \quad (2)$$

or $\mathbf{M}^{\mu a} = \mathbf{FM}'$, which can be solved using standard linear algebraic methods [10] to compute the image correction filter $\mathbf{F}$.

Subsequently, any image $\mathbf{m}'$ that is reconstructed using the same set of pixels and measurement geometry as used in the computation of $\mathbf{F}$ is corrected by calculating the matrix product $\mathbf{Fm}'$.

Intuitively it might seem that $N_p$, the length of the time series used in the filter generation process, needn't be any larger than $N_p$. In practice, it turns out (as shown subsequently in Fig. 12) that this approach performs best when $N_f \gg N_p$. For the examples presented here, we had $N_p$ = 982 or 984, and $N_f$ = 16384 (i.e., $2^{14}$). That is to say, practical implementation of the deconvolution strategy requires an ability to reconstruct many images in a reasonably short time.

### 2. Three-dimensional Target Media

The target media used for the demonstrations that are reported here of the efficacy of the linear deconvolution approach are the 3D finite element meshes shown in Figure 5. The hemispheric mesh shown in Fig. 5(a), which approximates the measurement geometry for DOT mammographic studies, contains 4309 tetrahedral elements, with 982 nodes; the curved slab mesh (Fig. 5(b)), which approximates the measurement geometry for DOT brain imaging, contains 4274 tetrahedral elements, with 984 nodes. The diameter of the hemisphere is 8.0 cm.

For the hemispheric mesh, 29 detector locations were designated (only 14 are visible in Fig. 5(a)), and 25 of these also were used as sources, for a total of 725 source-detector channels. For the curved slab mesh, 24 source and detector locations were designated, as shown in Fig. 5(b), for a total of 576 source-detector channels.

The patterns of static spatially heterogeneity used are shown in Figure 6. In these test media the inclusions are approximately spherical, with average diameters of 1.5 cm for the hemispheres and 1.2 cm for the curved slabs. The background regions of these media had uniform absorption, with $\mu_a$ = 0.06 cm$^{-1}$, while the inclusions were more strongly absorbing, with $\mu_a$ = 0.12 cm$^{-1}$ for the hemisphere and either 0.12 cm$^{-1}$ or 0.3 cm$^{-1}$ for the curved slab.

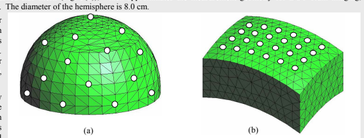


**Figure 5.** 3D FEM meshes, and source-detector geometries, used for computing and testing image deconvolution operators (filters). (a) – hemispheric mesh, containing 982 nodes and 4309 tetrahedral elements. (b) – curved-slab mesh, containing 984 nodes and 4274 tetrahedral elements. Source/detector locations are marked with small white circles.

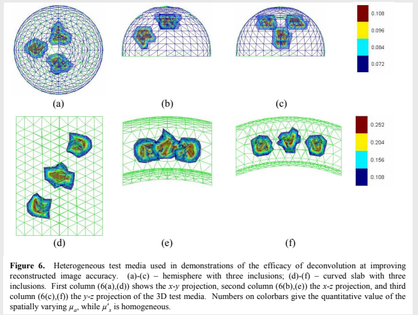


**Figure 6.** Heterogeneous test media used in demonstrations of the efficacy of deconvolution at improving reconstructed image accuracy. (a)-(c) – hemisphere with three inclusions; (d)-(f) – curved slab with three inclusions. First column (6(a),(d)) shows the *x*-*y* projection, second column (6(b),(e)) the *x*-*z* projection, and third column (6(c),(f)) the *y*-*z* projection of the 3D test media. Numbers on colorbars give the quantitative value of the spatially varying $\mu_a$, while $\mu'_s$ is homogeneous.

## RESULTS

The effectiveness of the linear deconvolution method presented here is shown for both the hemispheric (full tomographic measurement) and the curved-slab (limited view, back-reflection measurement) media. The ideal, noise-free case is treated first, then we consider the effect on the deconvolved solution of corrupting the detector data with multiplicative Gaussian noise. Then, because a basic premise of this work is that linear spatial convolution is a more important source of the errors in reconstructed DOT images than is the nonlinear relationships between a medium's optical parameters and DOT measurement data, the performance of the image correcting filter and a nonlinear iterative reconstruction algorithm are directly compared. Finally, we explore the dependence of the performance of a filter on the length $N_f$ of its generating image time series. This study demonstrates the validity of the condition given in Methods, that $N_f \gg N_p$ for optimal filter performance.

The FEM meshes used for computation of detector readings were finer than those used for generation of the **F** matrices and for subsequent image reconstruction (hemisphere: 2212 nodes, 10305 elements; curved slab: 2062 nodes, 8698 elements). Thus there was no simple inverse crime committed in the preparation of these results.

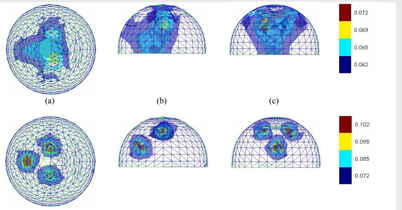


**Figure 7.** Reconstructed image of three-inclusion hemispheric test medium (see Fig. 6(a)-(c)). (a)-(c) – uncorrected image, solution to linear perturbation equation; (d)-(f) – corrected image, obtained by applying spatial deconvolution filter to the result in 7(a)-(c). First column (7(a),(d)) shows the *x*-*y* projection, second column (5(b),(e)) the *x*-*z* projection, and third column (5(c),(f)) the *y*-*z* projection of the 3D images. Numbers on colorbars give the quantitative value of the spatially varying $\mu_a$.

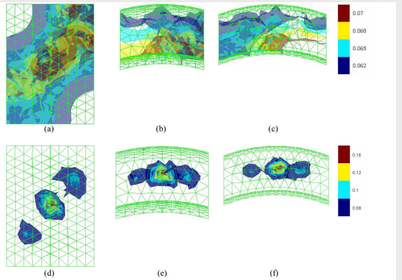


**Figure 8.** Reconstructed image of three-inclusion curved-slab test medium (see Fig. 6(d)-(f)). (a)-(c) – uncorrected image; (d)-(f) – corrected image, obtained by applying spatial deconvolution filter to the result in 8(a)-(c).

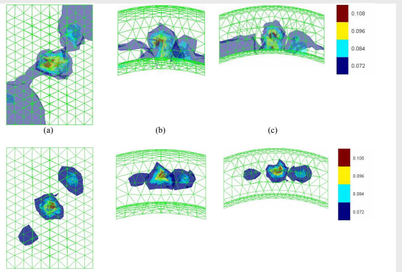


**Figure 11.** Comparison of performance of a nonlinear iterative image reconstruction algorithm and the spatial deconvolution approach. Test medium is curved slab with three inclusions (see Fig.6(d)-(f)); detector data are noise-free. (a)-(c) – image obtained after ten iterations (~90 min computation time) of a Levenberg-Marquardt nonlinear reconstruction algorithm [10]; (d)-(f) – corrected image, obtained by applying spatial deconvolution filter (~0.01 s computation time) to the result in 11(a)-(c).

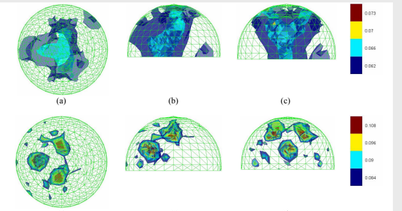


**Figure 9.** Reconstructed image of three-inclusion hemispheric test medium (see Fig. 6(a)-(c)), when detector data are corrupted with Gaussian noise, whose standard deviation for each detector channel is 1% of that channel's noise-free light intensity level. (a)-(c) – uncorrected image; (d)-(f) – corrected image, obtained by applying spatial deconvolution filter to the result in 9(a)-(c).

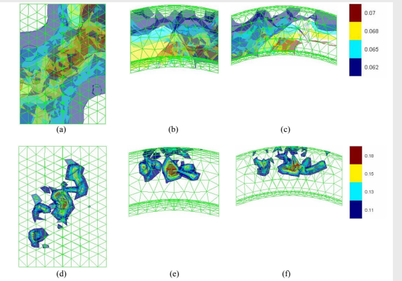


**Figure 10.** Reconstructed image of three-inclusion curved-slab test medium (see Fig. 6(d)-(f)), when detector data are corrupted with noise Gaussian noise, whose standard deviation for each detector channel is 1% of that channel's noise-free light intensity level. (a)-(c) – uncorrected image; (d)-(f) – corrected image, obtained by applying spatial deconvolution filter to the result in 10(a)-(c).

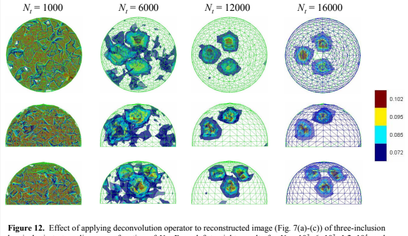


**Figure 12.** Effect of applying deconvolution operator to reconstructed image (Fig. 7(a)-(c)) of three-inclusion hemispheric test medium, as a function of $N_f$. From left to right, results for $N_f = 10^3$, $6\times10^3$, $1.2\times10^4$, and $1.6\times10^4$. Top row shows the *x*-*y* projection, middle row the *x*-*z* projection, and bottom row the *y*-*z* projection of the 3D images.

## CONCLUSIONS

1. Applying a linear spatial deconvolution operation to DOT images reconstructed by solving a first-order perturbation equation (Born approximation) can yield marked enhancement of image quality. These corrected (filtered) images are quantitatively accurate in terms of target location, size and shape. In the 3D examples that were considered here, use of image-correcting filters produced obvious improvement in image quality, in terms of both location and $\mu_a$ of the inclusions. The displacement between the true and recovered locations of an inclusion's centroid location were as small as 1 mm, in a 8-cm-diameter medium with 1.5-cm-diameter inclusions, and the peak value of the recovered $\mu_a$ for the inclusions deviated from the true value by as little as 5% (see Figs. 7,9). Multiple inclusions were present in all cases, and the spatial deconvolution strategy successfully resolved the inclusions while also accurately locating each one.

2. Corruption of the simulated detector data with multiplicative Gaussian noise (Figs. 9, 10) did not bring about reduction of spatial resolution or in the qualitative (centroid location) or quantitative (peak $\mu_a$ value) accuracy of the recovered inclusions. Thus it is reasonable to progress from simulation studies to tests involving laboratory phantoms, to determine whether the approach presented here is likewise robust to all of the forms of noise that are present in experimental data. The principal effect of the noise was the appearance of small, irregularly shaped regions of spurious absorption contrast. Notably, in the case where a back-reflection measurement was simulated (Fig. 9), the latter regions showed a pronounced depth dependence, decreasing in size and magnitude with increasing depth. This pattern suggests that it would be profitable to implement depth-dependent regularization when computing solutions to the inverse problem.

3. The quality of the results actually obtained, particularly in the direct comparison of spatial deconvolution and a nonlinear LM reconstruction algorithm (Fig. 11) implies that the information-spreading properties of the reconstruction algorithm are a primary cause of the low spatial resolution and depth bias commonly seen in DOT images. It is recognized that 10 almost certainly is not the optimum number of LM iterations; employing the optimal number of iterations would improve the quality of the result in Fig. 11(a)-(c), and the algorithm itself could probably be optimized to yield a higher rate of convergence. In any case, however, the post-measurement computational time and cost would invariably be many times greater for any approach of this type than for application of the image-correcting filter, which requires only a matrix multiplication.

4. This work suggests several directions for further development and improvement of the image-enhancement strategy. For one, it appears highly probable that a simultaneously fast and accurate "hybrid" reconstruction algorithm can be synthesized by applying spatial deconvolution and a nonlinear updating scheme in an alternating fashion. The resulting procedure should converge more rapidly than, say, the LM algorithm used to generate the results shown in Fig. 11, while also permitting recovery of media in which nonlinear effects of the optical coefficient perturbations are significant. A second important modification is to tag both the absorption and scattering coefficients of a medium simultaneously. The principal benefit of this is that the filter matrices thereby derived can be applied to the output of algorithms that provide simultaneous reconstruction of $\mu_a$ and $\mu'_s$. At the same time, it would constitute a mechanism for quantifying the extent of inter-parameter crosstalk associated with a given reconstruction algorithm, and for reducing its impact where it does occur. Such crosstalk can be regarded as another sort of information spread, one that occurs in optical-parameter space rather than in physical space. Then the same general strategy that is used to correct for the effects of a reconstruction algorithm's ISFs should also be able to reduce crosstalk artifacts. A third objective will be to search for non-sinusoidal forms for the tagging functions used in generating filter matrices, that are optimal in the sense of minimizing the $N_f$ that is needed in order to achieve successful spatial deconvolutions.

## REFERENCES

[1] V. A. Markel and J. C. Schotland, "Effects of sampling and limited data in optical tomography," *Applied Physics Letters* **81**(7), 1180–1182 (2002).
[2] H. L. Graber, R. L. Barbour, and Y. Pei, "Quantification and enhancement of image reconstruction accuracy by frequency encoding of spatial information," in OSA Biomedical Topical Meetings, OSA Technical Digest (Optical Society of America, Washington DC, 2002), pp. 635–637.
[3] Y. Pei, Y. Pei, H. L. Graber, and R. L. Barbour, "Normalized-constraint algorithm for minimizing inter-parameter crosstalk in DC optical tomography," *Optics Express* **9**, 97–109 (2001).
[4] C. H. Schmitz, M. Löcker, J. M. Lasker, A. H. Hielscher, and R. L. Barbour, "Instrumentation for fast functional optical tomography," *Review of Scientific Instruments* **73**, 429–439 (2002).
[5] H. L. Graber, Y. Pei, and R. L. Barbour, "Imaging of spatiotemporal coincident states by DC optical tomography," *IEEE Transactions on Medical Imaging* **21**, 852–866 (2002).
[6] J. W. Goodman, "Imaging in the Presence of Randomly Inhomogeneous Media," Chap. 8 in *Statistical Optics* (Wiley–Interscience, New York, 1985).
[7] C. L. Matson, "Deconvolution-based spatial resolution in optical diffusion tomography," *Applied Optics* **40**, 5791–5801 (2001).
[8] H. Hofer, L. Chen, Y. Yoon, B. Singer, Y. Yamauchi, and D. R. Williams, "Improvement in retinal image quality with dynamic correction of the eye's aberrations," *Optics Express* **8**, 631–643 (2001).
[9] Y. Pei, H. L. Graber, and R. L. Barbour, "Influence of systematic errors in reference states on image quality and on stability of derived information for DC optical imaging," *Applied Optics* **40**, 5755–5769 (2001).
[10] H. Jiang, Y. Xu, and N. Iftimia, "Experimental three-dimensional optical image reconstruction of heterogeneous turbid media," *Optics Express* **7**, 204–209 (2000).

## ACKNOWLEDGMENTS

This work was supported by the National Institutes of Health (NIH) under Grants R21-HL67387, R21-DK63692 and R41-CA96102, and by the US Army under Grant DAMD017-03-C-0018, and by the New York State Department of Health.

I look to ***THE DIFFUSION OF LIGHT*** and education as the resource to be relied on for ameliorating the condition, promoting the virtue, and advancing the happiness of man.

— Thomas Jefferson (1822)